Designing Spray-based 3D Printable Cementitious Materials with Fly Ash Cenosphere and Air Entraining Agent

Bing Lu[a, b], Ye Qian[a], Mingyang Li[a], Yiwei Weng[a,b], Kah Fai Leong[a], Ming Jen Tan[a], Shunzhi Qian[a,b,*]

[a]Singapore Centre for 3D Printing, School of Mechanical and Aerospace Engineering, Nanyang Technological University, 50 Nanyang Avenue, Singapore 639798, Singapore

[b]School of Civil and Environmental Engineering, Nanyang Technological University, 50 Nanyang Avenue, Singapore 639798, Singapore

Abstract:

3D printing is a novel construction method, which utilizes sequential deposition of printable material to build structures. It contributes to the automation in civil engineering and offers advantages of design, greenness and efficiency. Similarities between conventional spray technology and 3D printing indicate the feasibility of spray-based 3D printing, which could enhance the automation in vertical and overhead construction. However, low dimensional accuracy of sprayed profiles with conventional materials greatly affects the quality of spray-based 3D printing. This study contributes to the development of cementitious material to improve the dimensional accuracy of spray-based 3D printing. In this study, fly ash cenosphere and air entraining agent were introduced to obtain the optimal mixture design considering the delivery and deposition requirements. Subsequent spray tests show that the optimal mixture has the smallest splash width and most uniform material distribution among all the designed mixtures. Analysis of deposition process reveals that the distribution of sprayed material is closely related with its rheological properties, which could guide the future research work on spray-based printing of cementitious materials.

Key words:

Spray-based 3D printing; Cementitious material; Rheology; Fly ash cenosphere; Air entraining agent

*: Corresponding author, email address: szqian@ntu.edu.sg

1. Introduction

3D printing, also known as Additive Manufacturing (AM), is a method to build designed structures with sequential deposition of printable materials [1]. The 3D printing technology has quickly expanded to many industries, including building and construction in recent years [2-4]. Compared with conventional construction methods, 3D printing contributes to the automation in civil engineering and offers more design freedom, less waste material and less labor costs [5].

Spray of cementitious materials is a conventional construction technology in civil engineering. With the injection of high-pressure compressed air, the cementitious material is sprayed on substrates and gradually builds up [6]. Compared with the casting of material, spray offers an easier approach in vertical and overhead construction. The sprayed material could build up to certain thickness on vertical and overhead substrates, and it has good adherence to these substrates [7]. These advantages lead to many engineering applications of spray, e.g. tunnel lining, infrastructure repairment and slope retainment [7-9].

The spray technology shares many similarities with 3D printing of cementitious materials. Spray of cementitious materials could be divided into delivery and deposition phases. In the delivery phase, the material needs to be pumped to the spray nozzle and entangle with injected compressed air to spray. In the deposition phase, the newly sprayed material additively builds on the previously sprayed material to reach the designated build-up thickness. Similarly, 3D printing process also consists of delivery and deposition phases. In the delivery phase, the cementitious material is pumped to printing nozzle through the hose. In the deposition phase, the cementitious material is deposited layer-by-layer with the controlled movement of printing nozzle [10-13]. These similarities indicate the feasibility of spray-based 3D printing, which could further improve the degree of automation in vertical and overhead construction.

However, low dimensional accuracy of sprayed profiles with conventional materials greatly affects the quality of spray-based 3D printing. The sprayed cementitious materials have non-uniform distribution, and build-up thickness varies greatly at different spots of sprayed regions [8]. As a result, the cross sections of the sprayed structure are irregular. Necessary post-processing such as manual scraping is

required for rectification [8], which greatly increases labor costs and construction time. The low dimensional accuracy issue further limits utilization of spray in the construction of vertical decorative structure, where high precision is crucial.

In spray-based 3D printing, the accuracy issue of spray might be solved by system control and material development. The system control could be achieved by feedback-oriented adaptive control algorithm [14]. After the material is sprayed, the information of material distribution is detected by sensors to construct the real-time profile. It can then be compared with the designed profile to calculate the location and amount of additional material required. Afterwards, the information is further utilized to adjust printing parameters such as robotic arm movement. In addition to the system control, developing suitable cementitious material for spray-based 3D printing is also an option, which motivates the research of this study. Compared with the system control solution which requires sophisticated sensors and feedback control system, material-based approach may provide an alternative and cost-effective solution. With improved accuracy, it is possible to utilize spray to build decorative structure without post-processing, as can be seen in Fig. 1.

Fig. 1 NTU logo manufactured by overhead spray-based 3D printing

The paper discusses the material solution for spray-based 3D printing. As sprayed material needs to resist gravity-induced shear to build up, reducing fresh density should be the direct way to improve the distribution of sprayed material. The reduction of material density could be achieved by the addition of air entraining agent (AEA), incorporation of lightweight aggregate or elimination of fine aggregate in

the mixture [6]. Considering the size limitation of aggregates in 3D printing [15], the elimination of fine aggregate to form no-fine concrete is not applicable. In this study, AEA and fly ash cenosphere (FAC) were introduced for density reduction. FAC is a hollow spherical lightweight aggregate, which could be sourced from fire power plants [16, 17]. FAC could effectively decrease the material density and was widely used as lightweight filler in the previous studies [16, 18, 19].

The developed material also needs to meet the rheological requirements of delivery and deposition phases. Previous studies of 3D printing and spray have illustrated rheological requirement of delivery phase [20, 21]. However, there is limited study for deposition phase of spray. While there are some reports on the influence of rheology on maximum build-up thickness, very limited study is carried out to investigate the effect of rheological properties on material distribution. On the other hand, previous studies of rheological effect of AEA have conflicting results, and there is limited study of rheological effects of FAC. Therefore, rheological assessment is necessary for the mixtures with AEA and FAC incorporation.

This study develops a suitable cementitious mixture for spray-based 3D printing with uniform material distribution. Firstly, the mixtures with different AEA and FAC incorporation were designed. Fresh density and rheological properties were assessed, followed by a selection of optimal mixture with the consideration of delivery and deposition requirements. Afterwards, spray tests were carried out to study the material distribution. Based on the material performance in delivery and deposition phase, a suitable mixture for spray-based 3D printing was proposed. The mechanism of uniform distribution was discussed through the analysis of material deposition process.

2. Experiment Procedure

2.1 Material Preparation

Fig. 2 shows the scanning electron microscope (SEM) image of FAC. The true density of FAC is 0.80 g/cm^3. In the experiment design, silica sand was partially or fully substituted by FAC. As Table 1 shows, the substitution percentages were classified into three levels, i.e. 0, 50% and 100%. The AEA used in the research study is EMAL 10N (Sodium lauryl sulphate), which is in powder form and fully soluble to water. Similarly, the dosage of AEA was classified into three levels, i.e. 0, 0.1 g/L and 0.2 g/L. The

naming code is adopted in the following format: M-<FAC substitution percentage>-<dosage of AEA>, e.g. M-50%-0.1 refers to the mixture with 50% FAC substitution and 0.1 g/L AEA. Mix proportion of other ingredients was kept the same among all the mixtures. Particle size distribution of FAC, silica sand, cement, fly ash and silica fume can be found in Fig. 3. The superplasticizer used in this study was ADVA-181N from Grace Pte. Ltd.

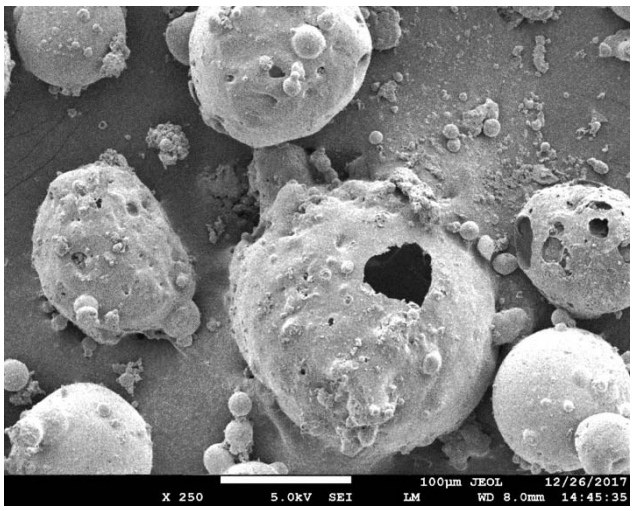

Fig. 2 SEM image of fly ash cenosphere (FAC)

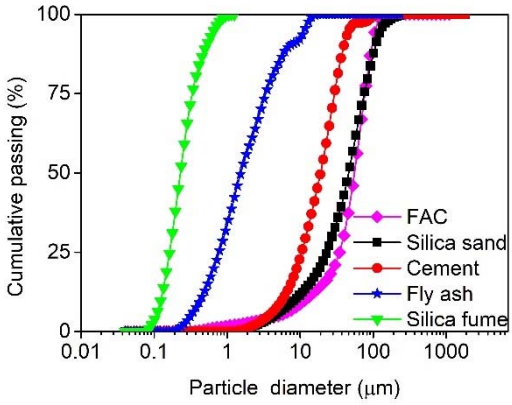

Fig. 3 Paritcle size distribution of FAC, silica sand, cement, fly ash and silica fume

Table 1 Mass proportion of mixtures

Mix	FA / C	SF / C	W / B	Agg. / B	Sp. / B	FAC / Agg.	AEA (g/L)
M-0-0						0%	0
M-50%-0						50%	0
M-100%-0						100%	0
M-0-0.1						0%	0.1
M-50%-0.1	0.50	0.05	0.40	0.29	0.35%	50%	0.1
M-100%-0.1						100%	0.1
M-0-0.2						0%	0.2
M-50%-0.2						50%	0.2
M-100%-0.2						100%	0.2

* Abbreviation: Agg.: aggregate (including silica sand and fly ash cenosphere); B: binder (including cement, fly ash, silica fume); FA: fly ash; C: cement; SF: silica fume; W: water; Sp.: superplasticizer; FAC: fly ash cenosphere; AEA: air entraining agent.

The material preparation process is illustrated as follows. Firstly, AEA is dissolved in the weighed water. All dry powder ingredients are mixed at low speed for 3 min. Then water (with AEA) is added and mixed at low speed for another 3 min. Superplasticizer is added afterwards, followed by the low-speed mixing for 1.5 min and high-speed mixing for 3 min. After completion of the aforementioned mixing process, the fresh material is ready for subsequent tests.

2.2 Material Characterization

2.2.1 Fresh density

As the material needs to resist the gravity-induced shear when sprayed on vertical walls or ceilings, it is critical to assess the fresh density. After material preparation, the fresh mixtures were filled into cubic moulds and weighed instantly. The fresh density values were calculated based on the measured weights and the volume of cubic moulds. For each mixture, three samples were assessed to obtain the average value and standard deviation of fresh density.

2.2.2 Workability

Flow table test is a frequently used method to intuitively assess the workability of extrusion-based 3D printable cementitious materials, which can be characterised by slump and flow diameter of the material [22, 23]. The flow table test was carried following ASTM C 1437 [24]. The fresh mixture was filled in the mini-slump cone, and the cone was quickly lifted to measure the slump of the mixture. Then the mixture was struck for 25 times to measure the flow diameter. Slump and flow diameter were measured every 15 minutes in an hour to track the time dependency of workability. Each test was repeated three times, based on which the average values and standard deviations of slump and flow diameter were calculated.

2.2.3 Rheological properties

The rheological properties of the fresh mixtures were measured using the Anton Paar Modular Compact Rheometer 102 (MCR 102). The protocols were designed to examine the plastic viscosity, dynamic yield stress and static yield stress of the fresh mixtures. A four-blade stirrer probe with a diameter of 30 mm and a height of 40 mm was used. The construction cell has a diameter of 70 mm. Each test was carried three times to obtain the average rheological parameters and corresponding standard deviations.

After material preparation, the fresh material was poured into the construction cell. Before each test, the material is hand tampered for 1 minute using a small whisk. Then the vane was quickly put in position and lowered to the designated position. The shearing protocols used in this study are presented in Fig. 4 and Fig. 5. After pre-shearing at 600 rpm for 240 s and resting for 60 s, either stepping down from 600, 500, 400, 300, 200 to 100 rpm for 60 s each or maintaining constant angular velocity at 0.1 rpm for 600 s was applied. The step-down protocol was used to measure the plastic viscosity and dynamic yield stress [25, 26] and the constant shear rate at 0.1 rpm was to measure the static yield stress [27]. The torque was recorded at 4 data points per second.

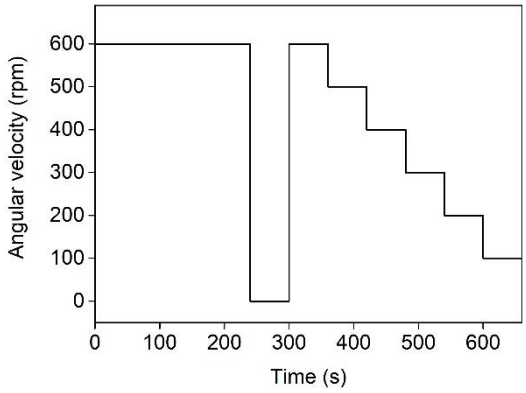

Fig. 4 Step-down shearing protocol

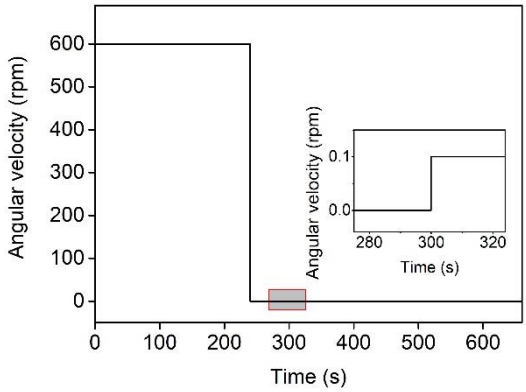

Fig. 5 Shear protocol to measure static yield stress

Using the step-down protocol, the equilibrium flow curve was thus obtained as the equilibrium torque vs. angular velocity. The equilibrium torque and angular velocity are commonly transferred to shear stress and shear rate respectively. In this study, the Reiner-Riwlin equation assuming Bingham behaviour for flow was adopted to obtain the equilibrium shear stresses and shear rates [28]. In the experiments, it was revealed that the equilibrium flow curves were quite linear and could fit well with Bingham model, as expressed by Eq. (1).

$$\tau=\tau_0+\mu\dot{\gamma} \tag{1}$$

where τ and $\dot{\gamma}$ are shear stress and shear rate respectively; τ_0 is the dynamic yield stress; μ is the plastic viscosity.

188 Under constant shear rate, the torque/shear stress increases to a peak value, then decay to an equilibrium
189 value [29]. The peak value is assumed to be the static yield stress [27]. It has been shown in many 3D
190 printing literatures that dynamic yield stress and plastic viscosity are related to pumpability; while static
191 yield stress is related to buildability [30].
192
193 **2.3.4 Spray performance**
194 Spray performance of cementitious materials could be greatly affected by process-related parameters,
195 e.g. the distance between the nozzle and substrate [31]. As this research study focuses on the development
196 of materials, it is necessary to keep constant process-related parameters to exclude their influence on
197 delivery and spray performance. In the spray tests, the air injection pressure was kept at 0.5 bar. The
198 MAI pictor pump was used with the constant pumping rate of 900 rpm (flow rate Q = 3.78 L/min). The
199 spray nozzle was connected to the pump by a hose of 2.5 m in length and 25.4 mm in diameter. After
200 material preparation, the fresh material was filled in the MAI pictor pump instantly. The material was
201 delivered through hose to the spray nozzle, and finally sprayed onto the substrates with the injected
202 compressed air. A six-axis robotic arm was introduced in the spray test to control the movement of the
203 nozzle. Setup of spray tests is displayed in Fig. 6.
204

205
206

Fig. 6 Setup of spray tests: (a) equipment setup; (b) details of spray nozzle

Fig. 7 illustrates the relative position of the spray nozzle and substrate. The spray nozzle was placed horizontally and perpendicular to the vertical substrate (*yz*-plane). Two types of spray tests were carried, i.e. single-layer spray and multiple-layer spray. The initial distance between the nozzle and the substrate was 50 mm. The mounted nozzle travelled along the *y*-axis for 445 mm at a speed of 100 mm/s to complete a single-layer filament. In the multiple-layer spray, the robotic arm quickly shifted backwards for 10 mm after completion of each layer, then moved in the opposite direction at the same speed to complete another layer. In this study, the number of layers in the multiple-layer spray is kept at three. After completion of designated layers, the sprayed filaments were covered with plastic sheets for 1 day. The filaments were scraped off from the substrate afterwards and cut to expose the cross-sections. Then the specimens were kept curing in the lab environment (temperature: 22.5 °C, relative humidity: 58%). Due to the acceleration and deceleration of the robotic arm near the endpoints of the filaments, the cross sections were cut at y = 100 mm, 150 mm and 200 mm respectively. The morphology and build-up thickness distribution were analyzed based on the three cross sections to assess the spray performance of the material.

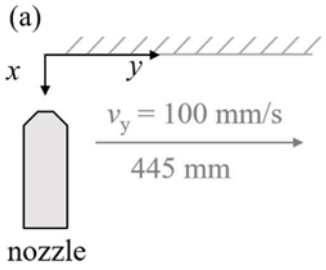

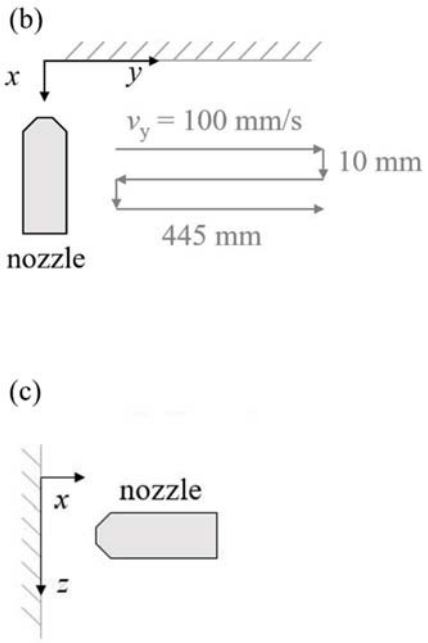

Fig. 7 Relative positions of spray nozzle and substrate: (a) top view of single-layer spray; (b) top view of multiple-layer spray; (c) side view of single-layer and multiple-layer spray

3. Assessment of Fresh Properties of Materials

3.1 Fresh Density

Fig. 8 shows the fresh density of designed mixtures. It could be found that the fresh density decreases with the increase in FAC substitution and dosage of AEA. The decreasing amounts are smaller when FAC substitution increases from 50% to 100%, or when the dosage of AEA rises from 0.1 g/L to 0.2 g/L. The significantly reduced fresh density illustrates the effectiveness of introducing FAC and AEA. In this study, with the combined incorporation of FAC and AEA, the fresh density could be reduced up to 38.5%.

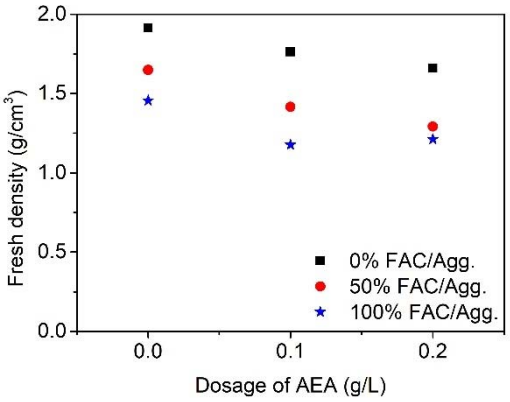

Fig. 8 Fresh density of designed mixtures

(the error bars are too small to be displayed)

3.2 Workability

The results of slump can be referred to in Fig. 9 and Fig. 10, while the results of flow diameter could be referred to in Fig. 11 and Fig. 12. It is revealed that the introduction of FAC and AEA leads to low slump values and spread diameter of fresh cementitious materials. This suggests the material could have better ability to retain the deposited shape [32] and hence possibly contributes to more uniform distribution of sprayed profile. However, the reduced slump values and spread diameter could also lead to poor pumpability of delivery [6]. The conflict in delivery and deposition performances requires further optimization and selection of suitable mixtures.

Furthermore, AEA tends to result in gentler decreasing or even stabilizing slump value/spread diameter with time. At the dosage of 0.2 g/L, the slump value/spread diameter almost remains constant within one hour. In contrast, large slump reduction could be observed in the mixtures without AEA. These mixtures show more than 40% and 16% reduction of initial slump and spread diameter after one hour, indicating the workability has high time dependence. The high time dependence of workability in the mixtures without AEA could affect the accuracy of printed profile, e.g. non-consistent dimensions of printed filament. Necessary real-time feedback-oriented adaptive adjustments are required, e.g. variable pumping rates to maintain the constant flow rate of the material for accuracy consideration and discontinuity prevention. However, using feedback-oriented adaptive spray printing system is not economical and even not applicable in some engineering applications. The mixture without AEA has

high time dependence of workability and hard to control, therefore no spray work was carried out for these mixtures.

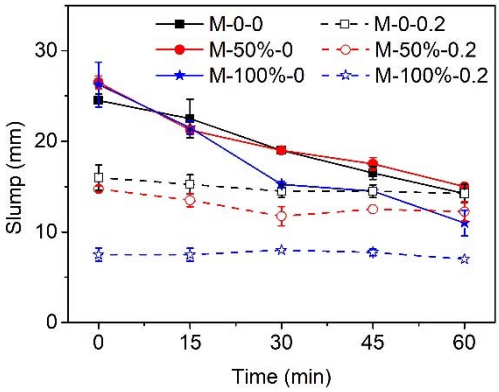

Fig. 9 Slump of mixtures with different FAC substitution percentage (Dosage of AEA: 0 g/L; 0.2 g/L)

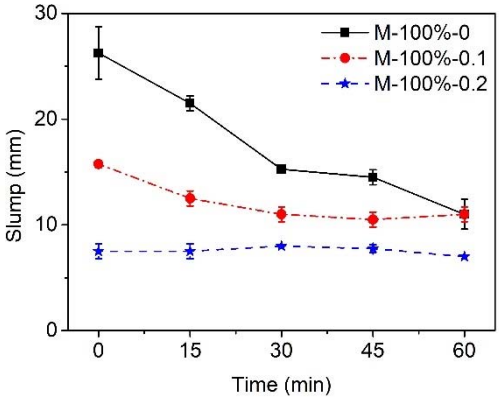

Fig. 10 Slump of mixtures with different dosage of AEA (FAC substitution percentage: 100%)

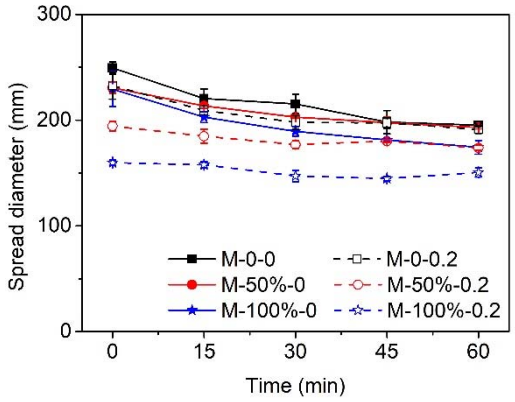

Fig. 11 Spread diameter of mixtures with different FAC substitution percentage (Dosage of AEA: 0 g/L; 0.2 g/L)

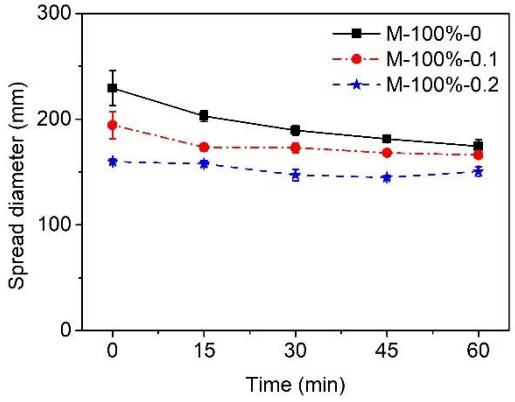

Fig. 12 Spread diameter of mixtures with different dosage of AEA (FAC substitution percentage: 100%)

3.3 Rheological Properties

Fig. 13 and Fig. 14 describe dynamic yield stress and plastic viscosity with respect to FAC substitution level and dosage of AEA. It is revealed that with the existence of AEA, the mixtures with 100% FAC substitution percentage has the lowest dynamic yield stress and plastic viscosity respectively. However, the effect of AEA on dynamic yield stress or plastic viscosity is inconclusive. For mixtures with 0% or 100% FAC substitution, dynamic yield stress decreases and then increases as the dosage of AEA increases from 0 to 0.2 g/L. In contrast, mixtures with 50% FAC substitution show the opposite trend. The plastic viscosity values of mixtures with 50% FAC substitution remain nearly constant, while

mixtures with 0% or 100% FAC substitution show non-consistent trends with increasing dosage of AEA. Among all the mixtures, M-100%-0.1 has the lowest dynamic yield stress and plastic viscosity.

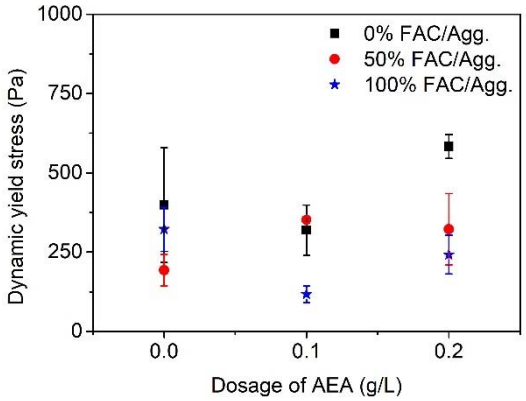

Fig. 13 Dynamic yield stress of designed cementitious materials

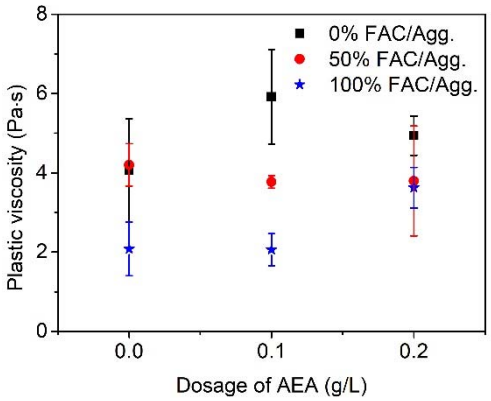

Fig. 14 Plastic viscosity of designed cementitious materials

Fig. 15 shows static yield stress with respect to FAC substitution level and dosage of AEA. It suggests that increasing substitution percentage of silica sand by FAC greatly decreases static yield stress. With FAC substitution percentage increasing from 0%, 50% to 100%, the increase of AEA generally leads to lower static yield stress. The decreasing trend is most pronounced with 100% FAC substitution.

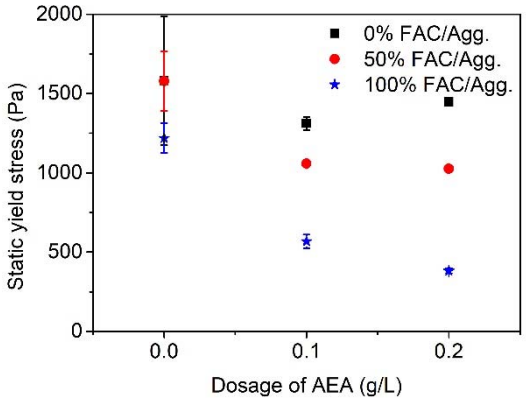

Fig. 15 Static yield stress of designed cementitious materials

3.4 Discussions

3.4.1 Analysis of fresh properties of materials

The information of dynamic yield stress and plastic viscosity could be further utilized to predict the pumping pressure in the delivery phase of spray-based 3D printing. Small pumping pressure indicates that the material is easier to be delivered. In contrast, large predicted pumping pressure indicates the requirement of more powerful pumping equipment and the printed profile may have discontinuities. With the constant flow of material in the hose, there exists pressure drop due to the internal friction and the friction between the material and the wall of hose. The relationship between pumping pressure P (Pa), radius of the hose R (m), length of the hose L (m) and volumetric flow rate Q (m^3/s) could be described as follows [33]:

$$P = \left(\frac{8\tau_0}{3R} + \frac{8\mu}{\pi R^4} Q \right) L \tag{2}$$

When pumping the material at constant flow rate Q, either increasing dynamic yield stress τ_0 or increasing plastic viscosity μ leads to higher pumping pressure, which is not desirable from the viewpoint of printing operation.

Based on Eq. (2), the pumping pressure for different mixtures was calculated to reflect their respective pumpability. The calculation has been carried out with the following parameters: R = 0.0127 m (0.5 inch); L = 2.5 m; Q = 3.78 L/min. All these parameters have been adopted in the subsequent spray test. The calculated pumping pressure is shown in Fig. 16. By comparing the trends when the dosage of AEA increases in Fig. 13, Fig. 14 and Fig. 16, it could be seen that the calculated pumping pressure is largely

hinged on the dynamic yield stress of the material. Alternatively, the same observation could be made using the following equation generated by Eq. (2), where all the coefficients have been calculated:

$$P = 0.00525\tau_0 + 0.15417\mu \quad (3)$$

where P, τ_0 and μ are in the unit of bar, Pa and Pa·s, respectively. With the variation of τ_0, P varies for about 2.44 bar. In contrast, with the variation of μ, P only varies for about 0.89 bar. This observation is contradictory to the case of extrusion-based 3D printable cementitious materials, where the pumping pressure is largely hinged on the plastic viscosity of the material [21]. The discrepancy could be attributed to the relatively small plastic viscosity of designed sprayable mixtures. Among all the designed mixtures, M-100%-0.1 has the lowest calculated pumping pressure.

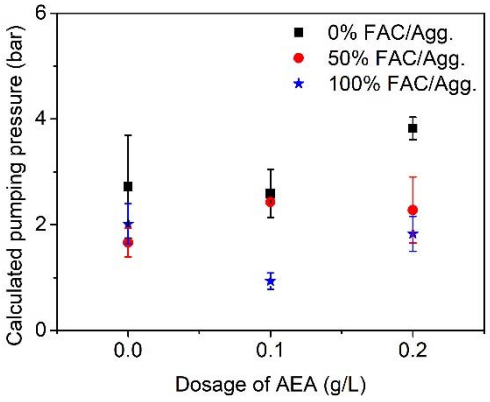

Fig. 16 Calculated pumping pressure of the designed mixtures

Recent studies revealed that static yield stress contributes to the buildability of deposited material [21, 34]. The maximum build-up thickness H (m) of extruded or sprayed material is found to have linear relationship with the ratio of static yield stress τ_s (Pa) to the product of fresh density ρ (kg/m^3) and gravitational acceleration g_0 (m/s^2) [20, 34], i.e.:

$$H \propto \frac{\tau_s}{\rho g_0} \quad (4)$$

Eq. (4) illustrates that the material with higher static yield stress and lower fresh density has higher maximum build-up thickness, indicating more layers could be printed and thus better buildability. Hence, in case of extrusion-based 3D printable cementitious materials, it is necessary to improve the ratio of ($\tau_s/(\rho g_0)$). In comparison, while it is also necessary to achieve high maximum build-up thickness in spray-

based 3D printing, the material distribution after deposition is more important. However, there is limited study on the relation between the distribution of sprayed material and rheological properties [20, 35]. As the material distribution focuses on the build-up thickness values over the spray range, it is reasonable to examine this ratio. It is inferred that material with the large ratio may have more uniform build-up thickness distribution and more regular cross section, as the sprayed material with higher buildability could better resist gravity-induced shear and does not influence the adjacent region.

Fig. 17 shows the ratios of ($\tau_s/(\rho g_0)$) for mixtures with AEA. It should be noted that although the mixtures with 0% FAC substitution percentage have high static yield stress, their relatively large density values bring down the ratios. In comparison, as mixtures with 50% and 100% FAC substitution percentages have very similar density, their ratios follow the trend of static yield stress.

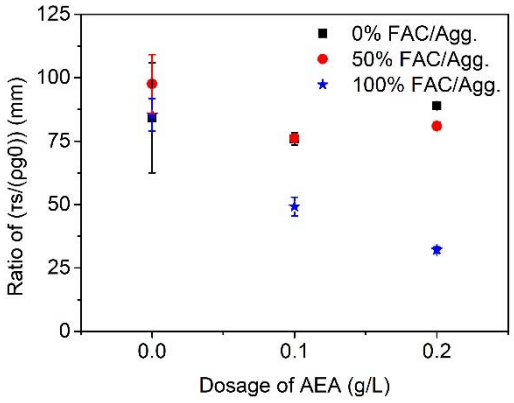

Fig. 17 Ratio of ($\tau_s/(\rho g_0)$)

3.4.2 Selection of the optimal mixture

Based on the necessity of low time dependence of workability which has been illustrated in Section 3.2, mixtures without AEA has been excluded from material selection. From the pumpability evaluation, M-100%-0.1 has the lowest calculated pumping pressure in the delivery phase. However, it also has a relatively small ratio of ($\tau_s/(\rho g_0)$), which could compromise the spray performance in the deposition phase. In comparison, M-0-0.1, M-50%-0.1, M-0-0.2 and M-50%-0.2 have large ratios of ($\tau_s/(\rho g_0)$), but they have much higher calculated pumping pressure than M-100%-0.1. As the material should achieve good performance in both delivery and deposition phases, a comprehensive material index Γ was proposed.

The material index Γ for each mixture is calculated in two steps. The first step is to normalize the calculated pumping pressure and the ratio of ($\tau_s/(\rho g_0)$). The normalization process follows a log-scale normalization procedure described as below [36]:

$$\tilde{A}_i = \frac{9}{\log \frac{A_{\max}}{A_{\min}}} \cdot \log \frac{A_i}{A_{\min}} \tag{5}$$

where $\tilde{A}_i$ and A_i are the normalized and original test results; $A_{\max}$ and $A_{\min}$ are the maximum and minimum test results. The second step is to assign weights and calculate the material index Γ. The weights are assigned 0.5 for each phase assuming equal importance for material performance in both delivery and deposition phases. As smaller pumping pressure is preferred, the coefficient of the calculated pumping pressure is set to be negative. Thus, the material index Γ_i for each mixture is calculated as follows:

$$\Gamma_i = -0.5\,\tilde{A}_{i,P} + 0.5\,\tilde{A}_{i,ratio} \tag{6}$$

where $\tilde{A}_{i,P}$ and $\tilde{A}_{i,ratio}$ are the normalized values for calculated pumping pressure and the ratio of ($\tau_s/(\rho g_0)$) respectively. Corresponding results are shown in Table 2.

Table 2 Material index Γ for mixtures with AEA

Mix	P (Pa)	Normalized P	($\tau_s/(\rho g_0)$) (mm)	Normalized ($\tau_s/(\rho g_0)$)	Γ
M-0-0.1	2.56	6.47	75.78	7.59	0.56
M-50%-0.1	2.43	6.14	76.19	7.64	0.75
M-100%-0.1	0.92	0	49.22	3.78	1.89
M-0-0.2	3.82	9	88.88	9.00	0
M-50%-0.2	2.22	5.57	80.97	8.18	1.30
M-100%-0.2	1.81	4.28	32.09	0.00	-2.14

From the table, it could be clearly seen that M-100%-0.1 has the largest material index value. Hence, it is regarded as the optimal material for spray-based 3D printing among all the mixtures. The material distribution of M-100%-0.1 was further assessed in the spray test. For comparison, the mixtures with small positive material index (M-0-0.1 and M-50%-0.1) and negative material index (M-100%-0.2) were selected for spray tests. In addition, M-0-0.1 and M-50%-0.1 have larger ratios of ($\tau_s/(\rho g_0)$), while M-100%-0.2 has smaller ratio of ($\tau_s/(\rho g_0)$).

4. Spray Performance Assessment

4.1 Morphology of Cross Sections

The morphology of cross sections was compared among the sprayed mixtures to offer the qualitative assessment of material distribution. Fig. 18 shows the representative cross sections of each mixture (cross sections cut at y = 150 mm of each filament). The cross sections were dyed with ink to highlight their morphology.

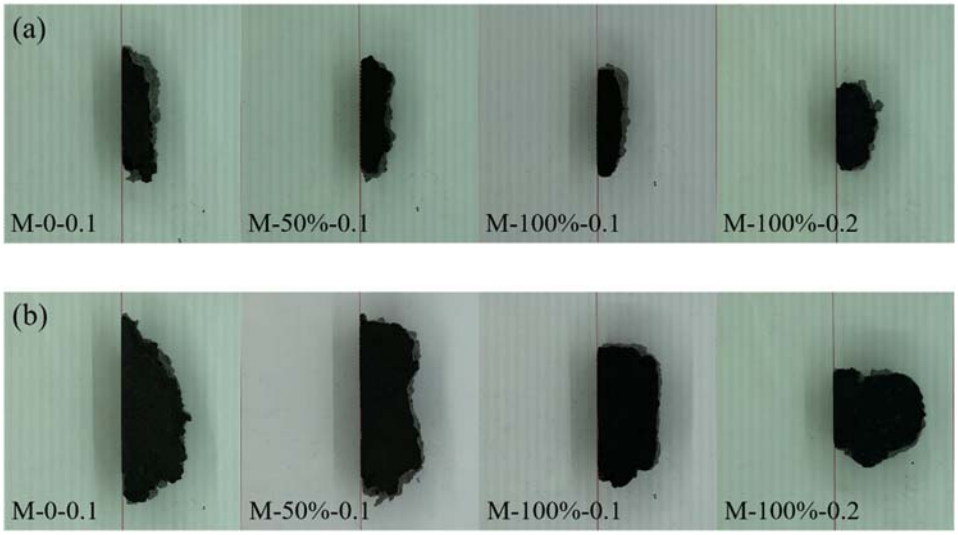

Fig. 18 Morphology of the representative cross sections of each mixture: (a) single-layer spray; (b) multiple-layer spray

It could be found that the mixture M-100%-0.1 has the most regular cross sections, especially in the multiple-layer spray. In comparison, other mixtures have distinctive irregular cross sections and non-uniform material distribution. The cross sections of M-0-0.1 and M-100%-0.2 show that the mixtures have significant offset to the lower side. In multiple-layer spray, the sprayed material of M-0-0.1 shows severe overall offset, while the sprayed material of M-100%-0.2 shows severe offset of the middle layer. The cross sections of M-50%-0.1 show concave curves near the centre in both single-layer spray and multiple-layer spray.

4.2 Build-up Thickness Distribution of Sprayed Filaments

The analysis of build-up thickness distribution was based on image processing of exposed cross sections [37]. It is complementary to the qualitative morphology assessment and offers a quantitative assessment of material distribution. However, the assessment of build-up thickness distribution cannot be applied to

M-100%-0.2 due to the offset-induced overhanging (see Fig. 18). For other mixtures, the build-up heights were measured at different locations indicated by z values. Zero z value is corresponding to the upper boundary of the sprayed filament, and the positive z-direction is pointing downwards on actual substrates. The build-up thickness distribution was depicted in Fig. 19 and Fig. 20.

Fig. 19 and Fig. 20 show the average material distribution of M-0-0.1, M-50%-0.1 and M-100%-0.1 in single-layer and multiple-layer spray respectively. M-100%-0.1 has slightly lower maximum build-up thickness compared with M-0-0.1 and M-50%-0.1, but the build-up thickness distribution of the material is more uniform, especially for multiple-layer spray. In multiple-layer spray, the build-up thickness distribution of M-100%-0.1 is more approaching isosceles trapezoid. A wide flat zone could be observed near the centre, where the build-up thickness varies very little. In contrast, the distribution of M-0-0.1 and M-50%-0.1 shows significant offset with more materials at the lower side. The build-up thickness has large variations near the centre in the mixture M-0-0.1 and M-50%-0.1. The improvement in material distribution could be further reflected by flat zone percentage and the standard deviation of thickness in the flat zone through least square analysis, as shown in Fig. 21. The average flat zone percentage in M-0-0.1 (multiple-layer spray) is 44.01% and the standard deviation of thickness in the flat zone is 1.87 mm. The average flat zone percentage in M-50%-0.1 (multiple-layer spray) is 73.46% and corresponding standard deviation is 2.77 mm. In comparison, the average flat zone percentage in M-100%-0.1 (multiple-layer spray) is 72.00% and the standard deviation of thickness in the flat zone is 1.01 mm. Hence the mixture M-100%-0.1 has the most uniform material distribution.

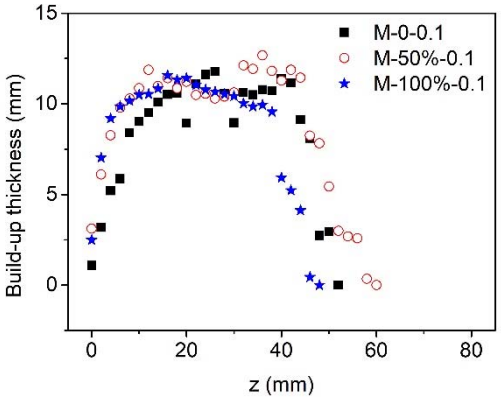

Fig. 19 Average material distribution of mixtures in single-layer spray

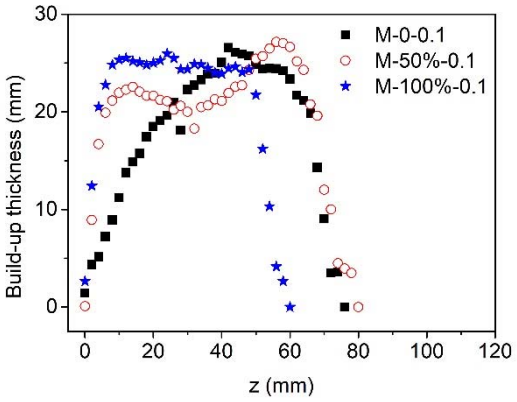

446

447 Fig. 20 Average material distribution of mixtures in multiple-layer spray

448

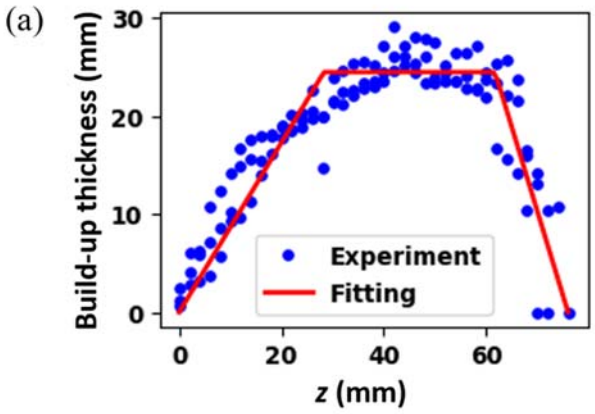

449

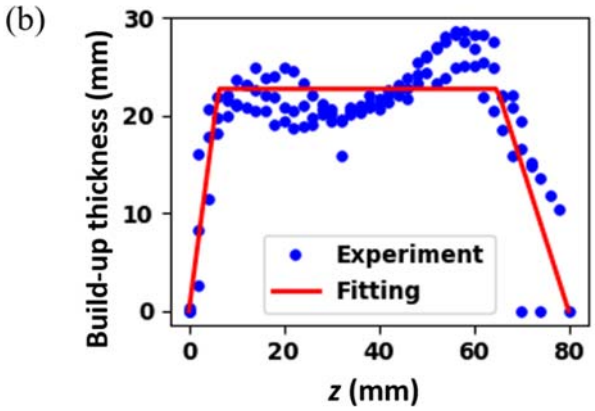

450

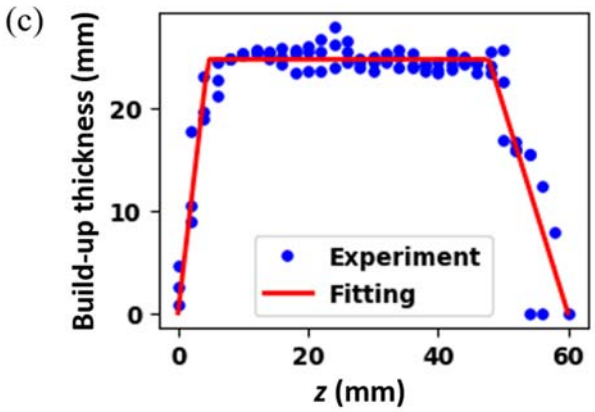

Fig. 21 Least sqaure analysis of material distribution (multiple-layer spray): (a) M-0-0.1; (b) M-50%-0.1; (c) M-100%-0.1

With the investigation of the morphology of cross sections and build-up thickness distribution, it is revealed that the mixture M-100%-0.1 has the best deposition performance. The sprayed filaments of the mixture have the most regular cross sections and most uniform build-up thickness distribution. In contrast, the sprayed filaments of other mixtures have severe offset, leading to irregular cross sections and non-uniform build-up thickness distribution.

The results do not fully agree with the assumption that material with larger ($\tau_s/(\rho g_0)$) has better spray performance. The mixture M-100%-0.2 has a lower ratio of ($\tau_s/(\rho g_0)$), which shows less uniform material distribution. The mixture M-0-0.1 and M-50%-0.1 have higher ratios of ($\tau_s/(\rho g_0)$), but also have less uniform distribution than M-100%-0.1. The discrepancy between the assumption and test results of material distribution is discussed in the following Section 4.3.

In the material selection, the mixture M-100%-0.1 with the largest material index is predicted to achieve the best balance between the delivery and deposition requirements, but not necessarily the best indiviual performance in both. However, the mixture shows the best performance in both delivery and deposition phases. The mixture M-100%-0.1 is confirmed the optimal mixture for spray-based 3D printing among all the mixtures in this study.

4.3 Discussions

The discrepancy in uniform material distribution should refer to the consideration of spray process. In the spray process, the material is projected at high speed on the substrate. The material may be compacted in the delivery and deposition, which lead to the change of actual volumetric flow rate. On the other hand, the deposition phase needs to be analysed, as the receiving impact pressure of projected material could lead to the change of material distribution.

The influence of compaction could be clearly seen in the analysis of build-up thickness. By comparing Fig. 19 and Fig. 20, it could be found that the average build-up thickness from multiple-layer spray was smaller than three times that of the single-layer spray. Table 3 shows the density of sprayed filaments of M-0-0.1, M-50%-0.1 and M-100%-0.1. It could be found that the 3-day density values of M-0-0.1 and M-50%-0.1 were smaller than their fresh density values, while M-100%-0.1 showed the opposite trend. In general, with the evaporation of water, the density in the lab environment should be smaller than fresh density. However, with the effect of pumping pressure, the material could be compacted and densified [20]. The compressibility of each mixture could be inferred by comparing the relative change of density, which is expressed in the following proposed equation:

$$\Psi = \frac{\rho' - \rho}{\rho} \tag{7}$$

where Ψ is defined as compressibility index, ρ' is the average value of 3-day density, and ρ is the average value of fresh density. High compressibility index suggests the material has been largely compacted. The compressibility index values were calculated and shown in Table 3. On the other hand, the actual volumetric flow rate could also be calculated by multiplying the cross section area of the sprayed filament and robotic arm moving speed in the single-layer spray. The actual volumetric flow rate was also included in Table 3.

Table 3 Density and compressibility index

Mixtures	M-0-0.1	M-50%-0.1	M-100%-0.1
3-day density (g/cm^3)	1.71 ± 0.12 (S) 1.62 ± 0.11 (M)	1.23 ± 0.02 (S) 1.34 ± 0.07 (M)	1.25 ±0.07 (S) 1.26 ± 0.01 (M)
Fresh density (g/cm^3)	1.76 ± 0.01	1.42 ± 0.02	1.18 ± 0.01

Compressibility index Ψ	-0.05	-0.10	0.06
Actual volumetric flow rate (L/min)	2.62	2.92	2.26

* Annotation: S: single-layer spray; M: multiple-layer spray. The 3-day density is measured in the lab environment (temperature: 22.5 °C, relative humidity: 58%).

The calculation of compressibility index reveals that M-50%-0.1 has the lowest compressibility index, while M-100%-0.1 has the highest compressibility index. Therefore, the actual volumetric flow rate of M-50%-0.1 was much larger than that of the M-0-0.1 and M-100%-0.1. With further regards to Fig. 13, the compressibility of the material seems to have the negative correlation with dynamic yield stress.

Fig. 22 shows the speed profile with spray angle α and an infinitesimal annulus at radius r on the substrate. For the speed profile, v_x is the speed in the direction perpendicular to the substrate and v_r is the speed in the direction paralleling to the substrate. The area of the infinitesimal annulus is $2\pi r\mathrm{d}r$. During the infinitesimal time dt, the mass through this annulus section dm could be calculated by:

$$dm = \rho \cdot 2\pi r dr \cdot v_x dt \tag{8}$$

The impulse of sprayed material dI could be further expressed as:

$$dI = v_x dm = \rho v_x^2 \cdot 2\pi r dr dt \tag{9}$$

Hence, the impact pressure by the material p could be calculated by:

$$p = \frac{dI}{2\pi r dr dt} = \rho v_x^2 < \tau_s \tag{10}$$

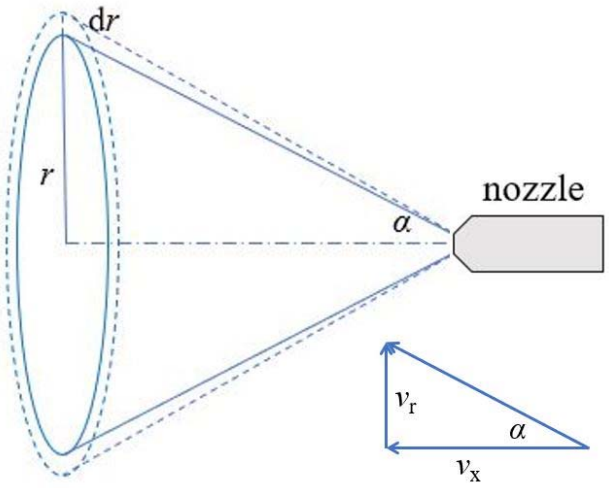

Fig. 22 Speed profile and locus of sprayed material

The impact pressure is balanced by the stress in the sprayed material. The lower volumetric flow rate of the material contributes to lower v_x and resultant lower impact pressure. Thus, M-100%-0.1 has the lowest v_x and impact pressure. Although M-50%-0.1 has higher static yield stress, the resultant higher impact pressure by the highest volumetric flow rate and density might exceed this value. In this situation, the sprayed material cannot preserve the original distribution and was forced to move. As a result, the distribution of M-50%-0.1 has the concave profile near the centre.

The sprayed filaments of M-0-0.1 does not have the concave profile, which may be attributed to its higher static yield stress and higher compressibility than those of M-50%-0.1. However, the material distribution of M-0-0.1 is also non-uniform. It could be found that more material tends to accumulate in the centre, and the filament also shifts a bit downwards. Some research studies suggested that the material with larger viscosity contributes to smaller spray angle [38, 39]. Hence, the material accumulation near the centre may be attribued to the small spray angle of M-0-0.1, while the examination of spray angle is required in further study.

The poor material distribution of M-100%-0.2 is due to the low ratio of ($\tau_s/(\rho g_0)$). As can be seen in the multiple-layer spray in Fig. 18, the sprayed filament has irregular cross section and non-uniform distribution. Other multiple-layer sprayed filaments of M-100%-0.2 also show the same trend. With a low $\tau_s/(\rho g_0)$, insufficient static yield stress cannot balance the gravity of large build-up.

With the analysis in this study, the selection criteria for spray-based 3D printable cementitious materials could be constructed. From the discussions in Section 3.4, low plastic viscosity and dynamic yield stress are preferred for the delivery phase of spray-based 3D printing. On the other hand, the material should have low plastic viscosity, dynamic yield stress, fresh density and high static yield stress for uniform material distribution.

5. Conclusions

The adoption of 3D printing contributes to automation, design freedom, greenness and efficiency in civil engineering. Conventional spray technology shares a number of similarities with 3D printing, indicating the feasibility of spray-based 3D printing. However, low dimensional accuracy of sprayed profiles with conventional materials greatly affects its quality, the error is typically in centimeter levels and necessary manual post-processing such as scraping must be applied [8]. This hinders the application of spray-based 3D printing and further automation in the building and construction field. The paper offers feasible material solution to improve its accuracy by incorporating fly ash cenosphere (FAC) and air entraining agent (AEA) in mixture design. The accuracy improvement of sprayed profile makes the designed mixture feasible for spray-based 3D printing, which could be further utilized for decorative structure without post-processing.

The assessment of fresh density and workability of designed mixtures reveals the effectiveness of introducing FAC and AEA. It is found that FAC and AEA could effectively reduce the fresh density of the mixture. In addition, increasing FAC substitution from 0 to 100% or increasing dosage of AEA from 0 to 0.2 g/L leads to smaller slump and flow diameter. The decrease of slump and spread diameter indicates the improved buildability with the incorporation of FAC and AEA in this study.

The addition of AEA tends to result in gentler decreasing or even stabilizing slump/spread diameter with time. At the dosage of 0.2 g/L, the slump/spread diameter remains nearly constant within one hour from mixing. In comparison, the mixtures without AEA show large decrease of slump/spread diameter, indicating high time dependency of workability. These mixtures were hard to control and thus not applicable for spray-based 3D printing assuming a feedback control system is not readily available.

Rheological tests were carried out to further predict the pumpability and deposition performance of designed mixtures. The results show that the mixture with 100% FAC substitution percentage and 0.1g/L AEA (referred to as M-100%-0.1) has the lowest dynamic yield stress and plastic viscosity, yet not too low static yield stress. Subsequent calculations point out the mixture has the lowest required pumping pressure, while it may compromise the deposition performance. A material index was proposed to evaluate the performance in both of delivery and deposition phases. The mixture with the highest material index is inferred as the optimal mixture for spray-based 3D printing, which should achieve the best balance between the requirements of delivery and deposition. Through the analysis of cross sections of sprayed filaments and build-up thickness distribution, the optimal mixture M-100%-0.1 was found to have the most uniform material distribution. In multiple-layer spray, the mixture M-100%-0.1 has large flat zone percentage (72.00%) with the lowest standard deviation of thickness in the flat zone (1.01 mm). In comparison, the mixture M-0-0.1 has much smaller flat zone percentage (44.01%) while the mixture M-50%-0.1 has much higher standard deviation of thickness in the flat zone (2.77 mm). It reveals that the optimal mixture could achieve the best performance in delivery and deposition respectively, rather than compromising each other.

The discussion of material deposition process reveals that the material distribution can be affected by many rheological properties. Through the comparison of changes in density, the material with lower dynamic yield stress seems to have higher compressibility. The optimal mixture M-100%-0.1 was mostly compacted in the spray process, leading to the lowest actual volumetric flow rate. The lowest resultant impact pressure of the optimal mixture explains its best deposition performance. The mixture with large plastic viscosity is found to obviously accumulate more material near the centre, which may be attributed to the induced small spray angle. In addition, the mixture with low ratio of static yield stress to the product of fresh density and gravitational acceleration ($\tau_s/(\rho g_0)$) has poor material distribution. The phenomenon could be attributed to the insufficient static yield stress for balancing the gravity of large build up.

With the analysis of delivery and deposition phases, the material design criteria for spray-based 3D printing were proposed. The suitable material should possess low plastic viscosity, dynamic yield stress

for better delivery performance and more uniform distribution of sprayed material; in addition, high static yield stress and low density are also required for good deposition performance. The proposed optimal mixture M-100%-0.1 in this study is suitable for spray-based 3D printing, which adopts 0.1 g/L AEA and 100% substitution of silica sand by FAC.

Acknowledgements

This research is supported by the National Research Foundation, Prime Minister's Office, Singapore under its Medium-Sized Centre funding scheme, Singapore Centre for 3D Printing and Sembcorp Design & Construction Pte Ltd.

References

[1] C.K. Chua, K.F. Leong, 3D Printing and Additive Manufacturing: Principles and Applications, World Scientific Publishing Co Inc, Singapore, 2017.
[2] B. Lu, M.J. Tan, S. Qian, A Review of 3D Printable Construction Materials and Applications, Proceedings of the 2nd International Conference on Progress in Additive Manufacturing, Research Publishing Services, Singapore, 2016, pp. 330-335.
[3] R. Buswell, W.L. de Silva, S. Jones, J. Dirrenberger, 3D printing using concrete extrusion: a roadmap for research, Cement and Concrete Research, 112 (2018) 37-49.
[4] T.A. Salet, Z.Y. Ahmed, F.P. Bos, H.L. Laagland, Design of a 3D printed concrete bridge by testing, Virtual and Physical Prototyping, 13 (2018) 222-236.
[5] D. Weinstein, P. Nawara, Determining the Applicability of 3D Concrete Construction (Contour Crafting) of Low Income Houses in Select Countries, Cornell Real Estate Review, 13 (2015) 94-111.
[6] A.M. Neville, Properties of concrete, Pearson, Harlow, England ; New York, NY, U.S., 2011.
[7] L. Luo, X. Li, M. Tao, L. Dong, Mechanical behavior of rock-shotcrete interface under static and dynamic tensile loads, Tunnelling and Underground Space Technology, 65 (2017) 215-224.
[8] ACI Committee 506, Guide to shotcrete / reported by ACI Committee 506 (ACI 506R-05), American Concrete Institute, Detroit, MI, U.S., 2005.
[9] P.K. Mehta, P.J.M. Monteiro, Concrete : microstructure, properties, and materials, McGraw-Hill, New York, NY, U.S., 2006.
[10] B. Khoshnevis, Automated construction by contour crafting—related robotics and information technologies, Automation in Construction, 13 (2004) 5-19.
[11] S. Lim, R.A. Buswell, T.T. Le, S.A. Austin, A.G.F. Gibb, T. Thorpe, Developments in construction-scale additive manufacturing processes, Automation in Construction, 21 (2012) 262-268.
[12] C. Jeffrey, Team of 3D-printing "Minibuilder" robots print large-scale structures on site, 2014.
[13] C. Gosselin, R. Duballet, P. Roux, N. Gaudillière, J. Dirrenberger, P. Morel, Large-scale 3D printing of ultra-high performance concrete–a new processing route for architects and builders, Materials and Design, 100 (2016) 102-109.
[14] H. Lindemann, R. Gerbers, S. Ibrahim, F. Dietrich, E. Herrmann, K. Dröder, A. Raatz, H. Kloft, Development of a Shotcrete 3D-Printing (SC3DP) Technology for Additive Manufacturing of Reinforced Freeform Concrete Structures, RILEM International Conference on Concrete and Digital Fabrication, Springer, Zurich, Switzerland, 2018, pp. 287-298.
[15] B. Panda, M. Li, Y.W.D. Tay, S.C. Paul, M.J. Tan, Modeling Fly Ash Based Geopolymer Flow for 3D Printing Applications, International Conference on Advances in Construction Materials and Systems, RILEM Publications S.A.R.L, Chennai, India, 2017, pp. 9-16.

[16] A. Hanif, Z. Lu, Z. Li, Utilization of fly ash cenosphere as lightweight filler in cement-based composites–a review, Construction and Building Materials, 144 (2017) 373-384.
[17] A. Hanif, Z. Lu, S. Diao, X. Zeng, Z. Li, Properties investigation of fiber reinforced cement-based composites incorporating cenosphere fillers, Construction and Building Materials, 140 (2017) 139-149.
[18] J.-Y. Wang, Y. Yang, J.-Y.R. Liew, M.-H. Zhang, Method to determine mixture proportions of workable ultra lightweight cement composites to achieve target unit weights, Cement and Concrete Composites, 53 (2014) 178-186.
[19] A. Hanif, S. Diao, Z. Lu, T. Fan, Z. Li, Green lightweight cementitious composite incorporating aerogels and fly ash cenospheres–Mechanical and thermal insulating properties, Construction and Building Materials, 116 (2016) 422-430.
[20] D. Beaupre, Rheology of high performance shotcrete, University of British Columbia, Vancouver, Canada, 1994.
[21] Y. Weng, M. Li, M.J. Tan, S. Qian, Design 3D printing cementitious materials via Fuller Thompson theory and Marson-Percy model, Construction and Building Materials, 163 (2018) 600-610.
[22] S.C. Paul, Y.W.D. Tay, B. Panda, M.J. Tan, Fresh and hardened properties of 3D printable cementitious materials for building and construction, Archives of Civil and Mechanical Engineering, 18 (2018) 311-319.
[23] Y. Zhang, Y. Zhang, G. Liu, Y. Yang, M. Wu, B. Pang, Fresh properties of a novel 3D printing concrete ink, Construction and Building Materials, 174 (2018) 263-271.
[24] C. ASTM, 1437-01. Standard Test Method for Flow of Hydraulic Cement Mortar, ASTM International, PA, U.S., 2001.
[25] Y. Qian, K. Lesage, K. El Cheikh, G. De Schutter, Effect of polycarboxylate ether superplasticizer (PCE) on dynamic yield stress, thixotropy and flocculation state of fresh cement pastes in consideration of the Critical Micelle Concentration (CMC), Cement and Concrete Research, 107 (2018) 75-84.
[26] Y. Qian, G.D. Schutter, Enhancing thixotropy of fresh cement pastes with nanoclay in presence of Polycarboxylate ether superplasticizer (PCE), Cement and Concrete Research, 111 (2018) 15-22.
[27] F. Mahaut, S. Mokéddem, X. Chateau, N. Roussel, G. Ovarlez, Effect of coarse particle volume fraction on the yield stress and thixotropy of cementitious materials, Cement and Concrete Research, 38 (2008) 1276-1285.
[28] M. Reiner, Deformation and flow: An elementary introduction to theoretical rheology, H.K. Lewis & Co. Ltd., London, 1949.
[29] Y. Qian, S. Kawashima, Distinguishing dynamic and static yield stress of fresh cement mortars through thixotropy, Cement and Concrete Composites, 86 (2018) 288-296.
[30] N. Roussel, Rheological requirements for printable concretes, Cement and Concrete Research, 112 (2018) 76-85.
[31] B. Lu, M. Li, W. Lao, Y. Weng, S. Qian, M.J. Tan, K.F. Leong, Effect of Spray-based Printing Parameters on Cementitious Material Distribution, Proceedings of Solid Freeform Symposium, Austin, TX, U.S., 2018, pp. 1989-2002.
[32] H. Hoornahad, Toward Development of Self-Compacting No-Slump Concrete Mixtures, Delft University of Technology, Delft, the Netherlands, 2014.
[33] R.P. Chhabra, J.F. Richardson, Non-Newtonian Flow and Applied Rheology: Engineering Applications, Butterworth-Heinemann, 2011.
[34] B. Khoshnevis, X. YUAN, B. Zahiri, J. Zhang, B. Xia, Deformation Analysis of Sulfur Concrete Structures Made by Contour Crafting, AIAA SPACE 2015 Conference and Exposition, AIAA SPACE Forum, Pasadena, CA, U.S., 2015, pp. 4452.
[35] B. Lu, M. Li, S. Qian, K.F. Leong, M.J. Tan, Develop Cementitious Materials Incorporating Fly Ash Cenosphere for Spray-based 3D Printing, Proceedings of the 3rd International Conference on Progress in Additive Manufacturing, Research Publishing Services, Singapore, 2018, pp. 38-43.
[36] D.W. Bunn, Analysis for optimal decisions, John Wiley & Sons, 1982.
[37] W. Lao, M. Li, L. Masia, M.J. Tan, Approaching Rectangular Extrudate in 3D Printing for Building and Construction by Experimental Iteration of Nozzle Design, Proceedings of Solid Freeform Symposium, Austin, TX, U.S., 2017, pp. 2612-2623.
[38] S. Chen, A. Lefebvre, J. Rollbuhler, Factors influencing the effective spray cone angle of pressure-swirl atomizers, Journal of Engineering for Gas Turbines and Power, 114 (1992) 97-103.
[39] P. Tinprabath, C. Hespel, S. Chanchaona, F. Foucher, Influence of biodiesel and diesel fuel blends on the injection rate and spray injection under cold conditions, ILASS–Europe 2014, 26th Annual Conference on Liquid Atomization and Spray System, Bremen, Germany, 2014.